

Research Article

Numerical Study of an Indicator Function for Front-Tracking Methods

Darae Jeong,¹ Seokjun Ham,² Junxiang Yang,³ Youngjin Hwang,² Soobin Kwak,² Haobo Hua,⁴ Xuan Xin,⁵ and Junseok Kim ²

¹Department of Mathematics, Kangwon National University, Chuncheon 24341, Gangwon-do, Republic of Korea

²Department of Mathematics, Korea University, Seoul 02841, Republic of Korea

³School of Computer Science and Engineering, Sun Yat-Sen University, Guangzhou 510275, China

⁴Department of Mathematics, Zhengzhou University of Aeronautics, Zhengzhou 450046, China

⁵Department of Mathematics, Harbin Institute of Technology at Weihai, Weihai 264209, China

Correspondence should be addressed to Junseok Kim; cfdkim@korea.ac.kr

Received 9 May 2022; Revised 17 June 2022; Accepted 4 July 2022; Published 31 July 2022

Academic Editor: Zhengbiao Peng

Copyright © 2022 Darae Jeong et al. This is an open access article distributed under the Creative Commons Attribution License, which permits unrestricted use, distribution, and reproduction in any medium, provided the original work is properly cited.

In this paper, we present a detailed derivation and numerical investigation of an indicator function for front-tracking methods. We use the discrete Dirac delta function to construct an indicator function from a set of Lagrangian points and solve the resulting discrete Poisson equation with the zero Dirichlet boundary condition using an iterative method. We present several computational tests to investigate the effect of parameters such as distance between points, uniformity of the distance, and types of the Dirac delta functions on the indicator function.

1. Introduction

Dirac delta function plays an important role in various scientific and industrial problems. One of them is on the numerical simulations of fluid flows including multiphase flows and fluid solid interaction (FSI) problems. The immersed boundary methods (IBM) are on the front burner for the numerical simulations of these problems and one of the key points lay on the methods to accurately separate the moving multiphase or solid boundaries. The phase field method (PHM) [1–4], level set method (LSM) [5–7], and volume of fluid methods (VOF) [8–10], express the different phases using particular scalar functions. These functions are designed to be advected by fluid flows and one phase changes to another one continuously to avoid numerical stability problem. It should be noted that the interphase is diffused and implicitly captured in the three methods. However, the immersed boundary method is different for its explicit boundary expression. Unlike PHM, LSM, and VOF, distinguish of different phase can be denoted directly by scalar phase

functions; in IBM, a so-called indicator function needs to be constructed for these phase distinctions indirectly. In this process, if a Dirac delta function is used for the construction of the indicator function, the diffused interaction forms as PHM, LSM, and VOF. From this point of view, these four methods are all belonged to diffused models in simulations of multiphase flows. In IBM, the fluid interface is explicitly represented by several Lagrangian points and the fluid flow is solved on a stationary Eulerian mesh. Furthermore, when solving Richards' equation [11, 12] for layered soils, the layers of soils can be expressed using an indicator function.

Multiphase fluid flows are important in various scientific and industrial problems. There are many mathematical models and numerical methods for the multiphase fluid flows such as the immersed boundary method (IBM) [13–16], level set method [5–7], phase-field method [1–4], volume of the fluid method [9, 10], and lattice Boltzmann method [17–20], to name a few.

In the front-tracking method [21] such as IBM, the fluid-fluid interface is represented by a Lagrangian grid and

the flow is solved on a stationary Eulerian mesh. The Lagrangian points are represented by a set of marker points and move with the fluid flow defined at the Eulerian grid. To represent viscosity or density difference between different fluids, and indicator function is calculated based on the marker points [21–23]. Therefore, the indicator function has an important role in not only theoretical issues coupling with the hydrodynamics equations [24], but also in practical approaches in recent studies. The density field was determined by the indicator function derived from an irrotational discrete delta vector in the droplet simulations with a large density ratio in [25]. To incorporate the viscoelasticity effect of Oldroyd-B fluid, the smoothed Heaviside indicator function was used for simulating the dynamics of Newtonian vesicle in [26]. The role of the indicator function was represented by the solid fraction in the diffuse-interface IB framework for conjugate-heat-transfer problems proposed by [27]. Moreover, the indicator function was used to identify the spatial distribution of physical quantities to predict the structure and refractive index profile of fiber-optic components in [28]. In [21], the authors presented the indicator function $I(x, y)$ based on a continuous version as follows:

$$I(x, y) = \int_A \delta(x - x') \delta(y - y') da', \quad (1)$$

where A is an area. Then, symbolically, we have the following equation:

$$\begin{aligned} \nabla I(x, y) &= \int_A \nabla(x - x') \delta(y - y') da', \\ &= - \int_A \nabla' \delta(x - x') \delta(y - y') da, \\ &= - \oint_{\partial A} \delta(x - x') \delta(y - y') n' da', \\ &= - \int_{\partial A} \delta(x - x') \delta(y - y') n' da', \end{aligned} \quad (2)$$

where n' is the outward unit normal vector at the domain boundary ∂A .

However, it is not straightforward to connect the relationship between the numerical scheme and the continuous version of the indicator function. Therefore, the objective of this paper is to present a detailed derivation and numerical investigation of the indicator function for front-tracking methods.

The paper is organized in the following manner. In Section 2, we present the detailed derivation of the indicator function. In Section 3, various numerical experiments are performed to investigate the effect of parameters such as distance between points, uniformity of the distance, and types of the Dirac delta functions on the indicator function. In Section 5, conclusions are drawn.

2. Derivation of the Indicator Function

Let $\delta(x)$ be a smoothed Dirac delta function and satisfy the following equation:

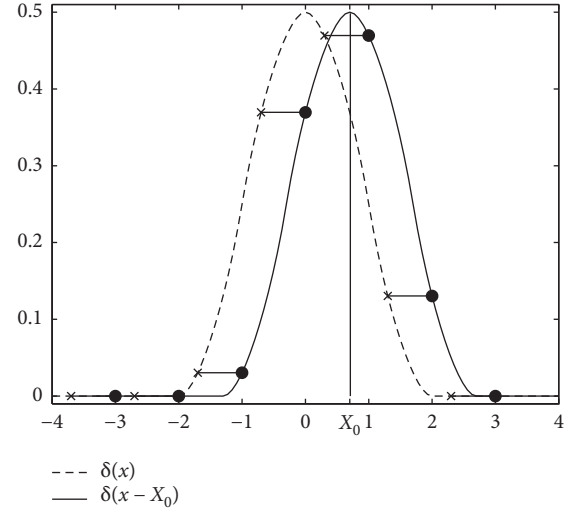


FIGURE 1: Schematic of delta function $\delta(x)$ and shifted delta function $\delta(x - X_0)$.

$$\int_{-\infty}^{\infty} \delta(x - x_0) dx = 1 \text{ for any } x_0 \in \mathbb{R}. \quad (3)$$

For example, a 4-point delta function [29–32] is given as follows:

$$\delta(x) = \frac{1}{h} \phi\left(\frac{x}{h}\right), \quad (4)$$

where h is the space step size in the discrete equation and given by the following equation:

$$\phi(r) = \begin{cases} \frac{(3 - 2|r| + \sqrt{1 + 4|r| - 4r^2})}{8}, & \text{if } |r| \leq 1, \\ \frac{(5 - 2|r| - \sqrt{-7 + 12|r| - 4r^2})}{8}, & \text{if } 1 \leq |r| \leq 2, \\ 0, & \text{otherwise} \end{cases} \quad (5)$$

Now, we consider a series of the shifted delta function $\delta(x - X_0)$ for some $-h < X_0 < h$ and it is shown in Figure 1 for some $X_0 = 0.7$ and $h = 1$, here we take $h = 1$ for better visualization. We describe the h effect in Section 3.1.

Let $x_i = ih$ for $i = \pm 1, \pm 2, \dots$. From the definition (4), we have the following equation:

$$\begin{aligned} \sum_{i=-\infty}^{\infty} h \delta(x_i - X_0) &= h \delta(x_{-2} - X_0) + h \delta(x_{-1} - X_0) \\ &\quad + h \delta(x_0 - X_0) + h \delta(x_1 - X_0) \\ &\quad + h \delta(x_2 - X_0) = 1. \end{aligned} \quad (6)$$

For any $X_0 \in \mathbb{R}$, $\sum_{i=-\infty}^{\infty} h \delta(x_i - X_0) = 1$ holds.

Let us consider a point $x = X_0$ at the interface in the one-dimensional space. We want to construct an indicator function which increases monotonically from zero to one across the point X_0 as x changes its position from left to right of the point, i.e.,

$$I(x) = \int_{-\infty}^x \delta(t - X_0) dt. \quad (7)$$

Figure 2 shows the delta function $\delta(x)$ (solid line) and the indicator function $I(x)$ (dashed line) with $h = 1$.

Taking a second derivative of equation (7) with respect to x , then we have the following equation:

$$I_{xx}(x) = \delta_x(x - X_0). \quad (8)$$

It implies that the indicator function can be found by solving the Poisson equation (8). Let us consider a 4-point delta function with $X_0 = 0$ and a discretization for equation (8) as follows:

$$I_{i+1} - 2I_i + I_{i-1} = \frac{(\delta_{i-1} - \delta_{i+1})}{2}, \quad (9)$$

where we have used the unit space step size $h = 1$ and $I_i = I(x_i) = I(i)$, $\delta_i = \delta(x_i) = \delta(i)$. Let $I_{-4} = 0$ and $I_4 = I_3$, then we can rewrite equation (9) for $i = -3, -2, \dots, 3$ as a matrix vector format:

$$\begin{pmatrix} -2 & 1 & 0 & 0 & 0 & 0 & 0 \\ 1 & -2 & 1 & 0 & 0 & 0 & 0 \\ 0 & 1 & -2 & 1 & 0 & 0 & 0 \\ 0 & 0 & 1 & -2 & 1 & 0 & 0 \\ 0 & 0 & 0 & 1 & -2 & 1 & 0 \\ 0 & 0 & 0 & 0 & 1 & -2 & 1 \\ 0 & 0 & 0 & 0 & 0 & 1 & -1 \end{pmatrix} \begin{pmatrix} I_{-3} \\ I_{-2} \\ I_{-1} \\ I_0 \\ I_1 \\ I_2 \\ I_3 \end{pmatrix} = \begin{pmatrix} \frac{\delta_{-2} - \delta_{-4}}{2} \\ \frac{\delta_{-1} - \delta_{-3}}{2} \\ \frac{\delta_0 - \delta_{-2}}{2} \\ \frac{\delta_1 - \delta_{-1}}{2} \\ \frac{\delta_2 - \delta_0}{2} \\ \frac{\delta_3 - \delta_1}{2} \\ \frac{\delta_4 - \delta_2}{2} \end{pmatrix}. \quad (10)$$

By multiplying both sides by the inverse of the coefficient matrix, we have the following equation:

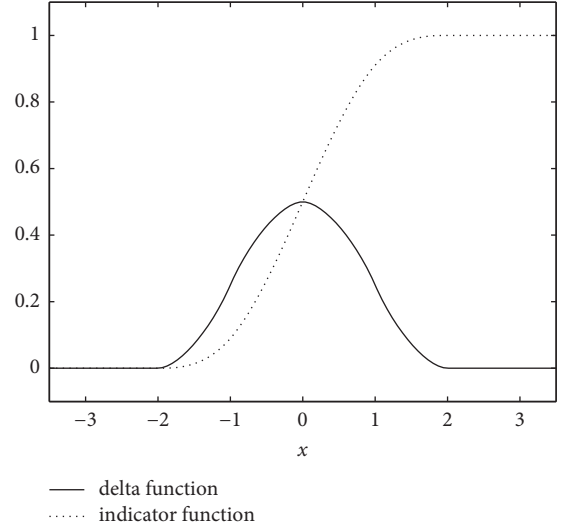


FIGURE 2: Delta function $\delta(x)$ (solid line) and indicator function $I(x)$ (dashed line) with $h = 1$.

$$\begin{pmatrix} I_{-3} \\ I_{-2} \\ I_{-1} \\ I_0 \\ I_1 \\ I_2 \\ I_3 \end{pmatrix} = \begin{pmatrix} -1 & -1 & -1 & -1 & -1 & -1 & -1 \\ -1 & -2 & -2 & -2 & -2 & -2 & -2 \\ -1 & -2 & -3 & -3 & -3 & -3 & -3 \\ -1 & -2 & -3 & -4 & -4 & -4 & -4 \\ -1 & -2 & -3 & -4 & -5 & -5 & -5 \\ -1 & -2 & -3 & -4 & -5 & -6 & -6 \\ -1 & -2 & -3 & -4 & -5 & -6 & -7 \end{pmatrix} \begin{pmatrix} \frac{\delta_{-2} - \delta_{-4}}{2} \\ \frac{\delta_{-1} - \delta_{-3}}{2} \\ \frac{\delta_0 - \delta_{-2}}{2} \\ \frac{\delta_1 - \delta_{-1}}{2} \\ \frac{\delta_2 - \delta_0}{2} \\ \frac{\delta_3 - \delta_1}{2} \\ \frac{\delta_4 - \delta_2}{2} \end{pmatrix}. \quad (11)$$

From equation (11), we obtain the following results:

$$\begin{aligned} I_{-3} &= \frac{1}{2} (\delta_{-4} + \delta_{-3} - \delta_3 - \delta_4) = 0, \\ I_i &= \frac{1}{2} \delta_i + \sum_{j=-2}^{i-1} \delta_j \text{ for } i = -2, -1, 0, 1, 2, \\ I_3 &= \delta_{-2} + \delta_{-1} + \delta_0 + \delta_1 + \delta_2 = 1, \end{aligned} \quad (12)$$

where we have used $\delta_{-4} = \delta_{-3} = \delta_3 = \delta_4 = 0$. Since $\delta(x) \geq 0$, the indicator function $I(x)$ is a monotonically increasing

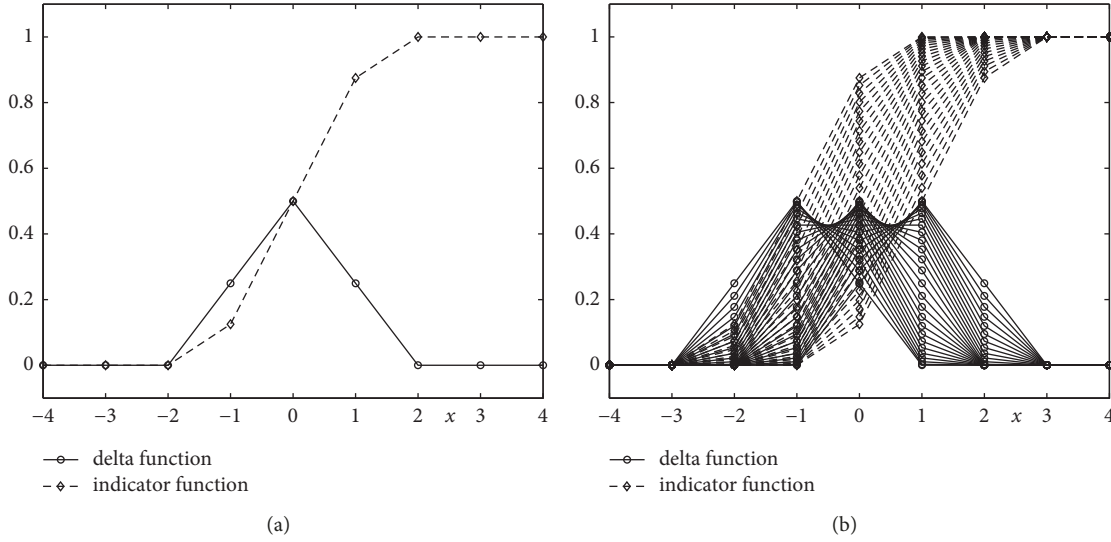


FIGURE 3: (a) Delta function $\delta(x)$ (solid line) and indicator function $I(x)$ (dashed line) with $X_0 = 0$. (b) Discrete delta and indicator functions with various point positions, $-1 < X_0 < 1$.

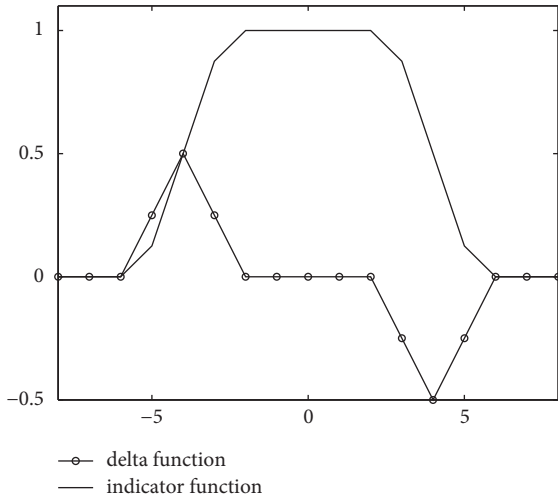


FIGURE 4: Sum of the Dirac delta functions $\delta(x + 4) - \delta(x - 4)$ and the associated indicator function $I(x)$.

function, i.e., $0 = I_{-4} = I_{-3} \leq I_{-2} \leq \dots \leq I_3 = I_4 = 1$. Figure 3(a) shows discrete delta function $\delta_{-4} = \delta_{-3} = \delta_{-2} = \delta_2 = \delta_3 = \delta_4 = 0, \delta_{-1} = \delta_1 = 0.25, \delta_0 = 0.5$ and discrete indicator function $I_{-4} = I_{-3} = I_{-2} = 0, I_{-1} = 0.125, I_0 = 0.5, I_1 = 0.975, I_2 = I_3 = I_4 = 1$ obtained from equation (12). Figure 3(b) shows discrete delta and indicator functions with various point positions, $-1 < X_0 < 1$.

Next, let us consider a hat shaped indicator function as shown in Figure 4 and the sum of the corresponding Dirac delta functions is $\delta(x + 4) - \delta(x - 4)$. If we solve the following equation for the indication function with zero Dirichlet boundary condition, then we have the result in Figure 4.

$$I_{xx}(x) = \delta_x(x + 4) - \delta_x(x - 4). \quad (13)$$

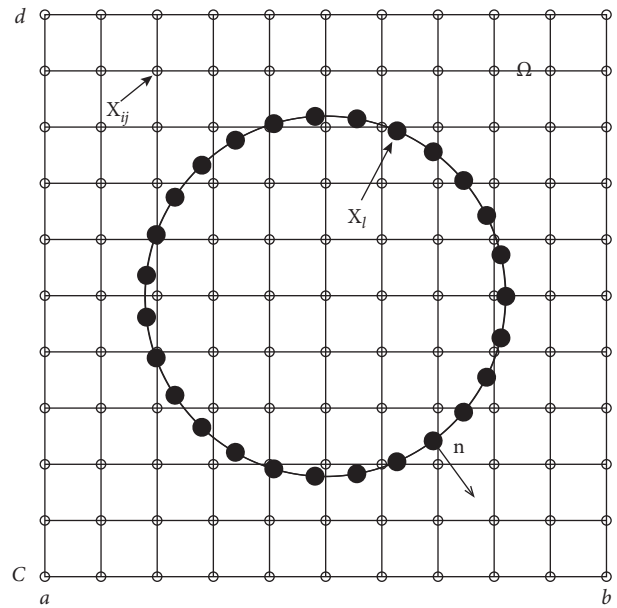


FIGURE 5: Eulerian points \mathbf{x}_{ij} , Lagrangian points \mathbf{X}_l , and normal vector \mathbf{n} for Lagrangian points in the computational domain $\Omega = (a, b) \times (c, d)$.

Now, we consider this in the two-dimensional space. Let a computational domain $\Omega = (a, b) \times (c, d)$ be partitioned in Cartesian geometry. Let N_x and N_y be the number of cells in the x - and y -directions, respectively. We assume a uniform mesh with mesh spacing $h = (b - a)/N_x = (d - c)/N_y$. Let $\mathbf{x}_{ij} = (x_i, y_j) = (a + ih, c + jh)$ for $i = 0, \dots, N_x$ and $j = 0, \dots, N_y$. Let $\mathbf{X}_l = (X_l, Y_l)$ for $l = 1, \dots, M$ be a set of M Lagrangian points, see Figure 5.

Because $I(\mathbf{x})$ is an indicator function, the following equation holds at the transition layer of the function:

$$\frac{\nabla I(\mathbf{x})}{|\nabla I(\mathbf{x})|} = -\mathbf{n}(\mathbf{x}), \quad (14)$$

where $\mathbf{n}(\mathbf{x})$ is the outward normal vector at \mathbf{x} . Next, let us rewrite equation (14) as follows:

$$\nabla I(\mathbf{x}) = -\mathbf{n}(\mathbf{x})|\nabla I(\mathbf{x})|. \quad (15)$$

We replace $\mathbf{n}(\mathbf{x})|\nabla I(\mathbf{x})|$ in equation(14). by $\sum_{l=1}^M \mathbf{n}(\mathbf{X}_l)\delta(\mathbf{x} - \mathbf{X}_l)\Delta s_l$, then we have the following equation:

$$\nabla I(\mathbf{x}) = -\sum_{l=1}^M \mathbf{n}(\mathbf{X}_l)\delta(\mathbf{x} - \mathbf{X}_l)\Delta s_l, \quad (16)$$

where $\delta(\mathbf{x} - \mathbf{X}_l) = \delta(x - X_l)\delta(y - Y_l)$ and $\Delta s_l = 0.5(|\mathbf{X}_{l+1} - \mathbf{X}_l| + |\mathbf{X}_{l-1} - \mathbf{X}_l|)$. After taking the divergence operator to equation (16), we have the following Poisson's equation:

$$\Delta I(\mathbf{x}) = \nabla \cdot \nabla I(\mathbf{x}) = -\nabla \cdot \left(\sum_{l=1}^M \mathbf{n}(\mathbf{X}_l)\delta(\mathbf{x} - \mathbf{X}_l)\Delta s_l \right). \quad (17)$$

We solve equation (17). with appropriate Dirichlet boundary condition. In this study, we use the Gauss–Seidel method.

3. Numerical Experiments

Let us consider two-dimensional indicators on the computational domain, $\Omega = (-4, 4) \times (-4, 4)$ with $h = 1$. In Figures 6 and 7, we consider uniform distance change of

y -direction, Δs for fixed $X_0 = 0$. In the immersed boundary method, there are many types of delta functions. Most commonly used delta functions are 2-point [31–33], 3-point [31, 32, 34], 4-point [29–32], 4-point cosine [30, 32], and 6-point [29, 31, 35, 36] functions. These functions are defined as follows:

(i) 2-point delta function [31–33]:

$$\phi(r) = \begin{cases} 1 - |r|, & \text{if } |r| \leq 1, \\ 0, & \text{otherwise.} \end{cases} \quad (18)$$

(ii) 3-point delta function [31, 32, 34]:

$$\phi(r) = \begin{cases} \frac{1}{3} \left(1 + \sqrt{-3r^2 + 1} \right), & \text{if } |r| \leq 0.5, \\ \frac{1}{6} \left(5 - 3|r| - \sqrt{-3(1 - |r|)^2 + 1} \right), & \text{if } 0.5 < |r| \leq 1.5, \\ 0, & \text{otherwise.} \end{cases} \quad (19)$$

(iii) 4-point cosine delta function [30, 32]:

$$\phi(r) = \begin{cases} \frac{1}{4} \left(1 + \cos\left(\frac{\pi r}{2}\right) \right) & \text{if } |r| \leq 2, \\ 0 & \text{otherwise.} \end{cases} \quad (20)$$

(iv) 6-point delta function [29, 31, 35, 36]:

$$\phi(r) = \begin{cases} \frac{61}{112} - \frac{11}{42}|r| - \frac{11}{56}|r|^2 + \frac{1}{12}|r|^3 \\ + \frac{\sqrt{3}}{336} \left(243 + 1584|r| - 748|r|^2 - 1560|r|^3 + 500|r|^4 + 336|r|^5 - 112|r|^6 \right) & \text{if } |r| \leq 1, \\ \frac{21}{16} + \frac{7}{12}|r| - \frac{7}{8}|r|^2 + \frac{1}{6}|r|^3 - \frac{3}{2}\phi(|r| - 1)^{1/2} & \text{if } 1 < |r| \leq 2, \\ \frac{9}{8} - \frac{23}{12}|r| + \frac{3}{4}|r|^2 - \frac{1}{12}|r|^3 + \frac{1}{2}\phi(|r|) & \text{if } 2 < |r| \leq 3, \\ 0 & \text{otherwise.} \end{cases} \quad (21)$$

Figure 6 shows 2-point, 3-point, 4-point, 4-point cosine, and 6-point delta functions from top to bottom row with $\Delta s = 1$. Figures 6(a)–6(d) are 2D delta function $\delta(\mathbf{x} - \mathbf{X}_0) = \delta(x - X_0)\delta(y - Y_0)$ with $X_0 = 0$ and $Y_0 = 0$; 2D delta functions $\delta(\mathbf{x} - \mathbf{X}_l) = \delta(x - X_l)\delta(y - Y_l)$ with $X_l = 0$ and various point positions with one distance; sum of 2D delta functions $\sum_l \delta(\mathbf{x} - \mathbf{X}_l)$; and 2D indicator function $I(\mathbf{x})$,

respectively. We obtain very similar results of indicator functions $I(\mathbf{x})$ for all cases except the 2-point delta function. Figure 7 shows the result of delta functions, the sum of delta functions, and indicator functions according to different $\Delta s = h, 2h, 3h$, respectively. As shown in Figure 7, in cases of $\Delta s = h$ and $\Delta s = 2h$, the indicator functions are similar. On the other hand, when $\Delta s = 3h$, the indicator function seems

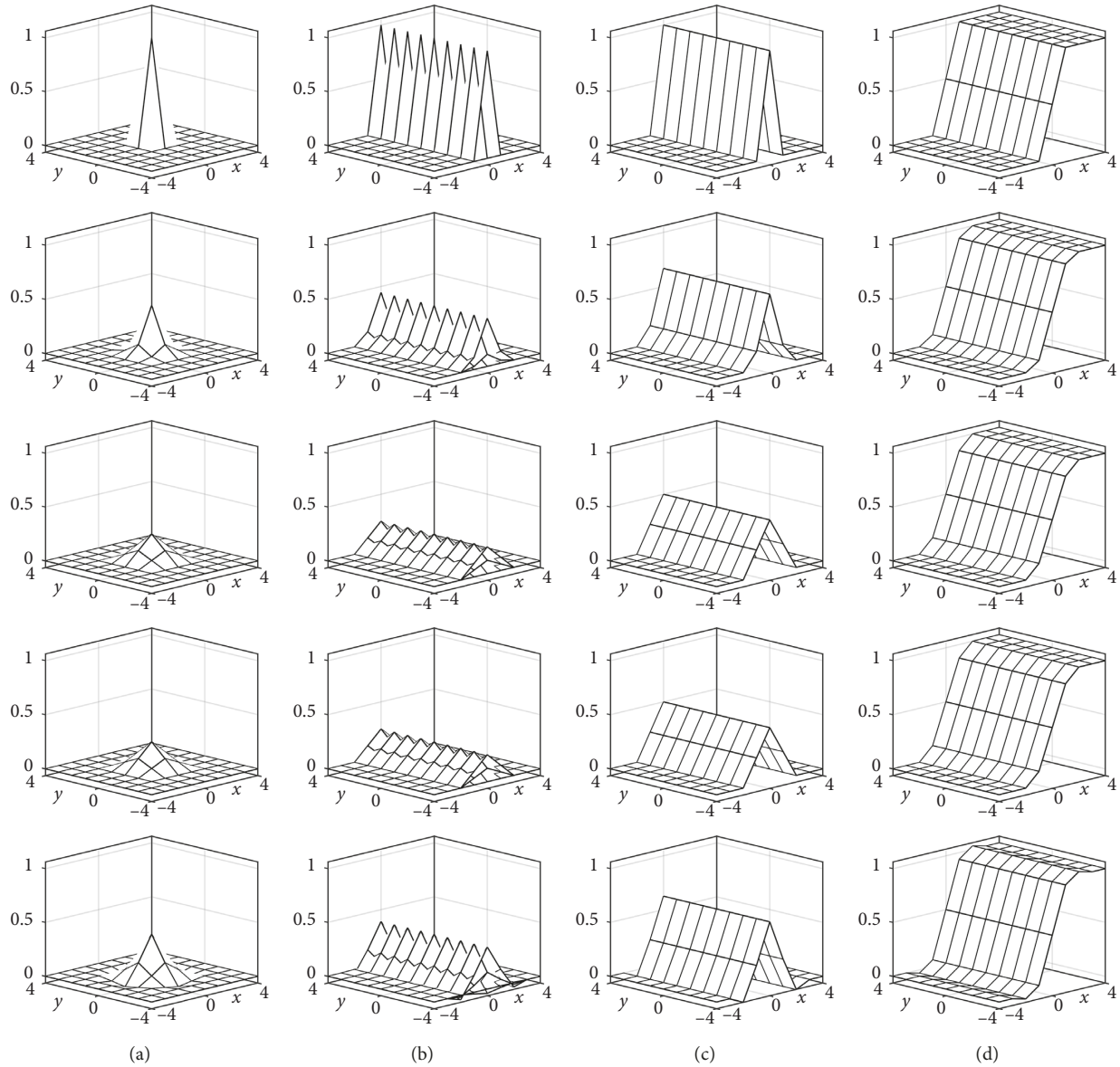


FIGURE 6: From top to the bottom row, 2-point, 3-point, 4-point, 4-point cosine, and 6-point delta functions: (a) 2D delta function $\delta(\mathbf{x} - \mathbf{X}_0) = \delta(x - X_0)\delta(y - Y_0)$ with $X_0 = 0$ and $Y_0 = 0$, (b) 2D delta functions $\delta(\mathbf{x} - \mathbf{X}_l) = \delta(x - X_l)\delta(y - Y_l)$ with $X_l = 0$ and various point positions with one distance, (c) sum of 2D delta functions $\sum_l \delta(\mathbf{x} - \mathbf{X}_l)$, and (d) 2D indicator function $I(\mathbf{x})$.

unstable compared to Figures 7(a) and 7(b). For this reason, it is recommended to use Δs which is at least smaller than $2h$ for a stable indicator function construction.

Let us consider an indicator on the computational domain, $\Omega = (-15, 15) \times (-15, 15)$ with $h = 1$ using the 4-point delta function. Figure 8 shows immersed boundary positions as a circle with different uniform distance Δs , 2D delta functions $\delta(\mathbf{x} - \mathbf{X}_l) = \delta(x - X_l)\delta(y - Y_l)$, $l = 1, 2, \dots, M$, the sum of 2D delta functions $\sum_l \delta(\mathbf{x} - \mathbf{X}_l)$, and 2D indicator function $I(\mathbf{x})$ from top to bottom row. We can observe that if Δs is too large, then the result of the indicator function is not good.

The first and second columns in Figure 9 show the construction of the indicator functions with randomly

distributed points ranging $0.5h < \Delta s_l < 1.5h$ and $2.5h < \Delta s_l < 4h$, respectively. We can observe that the indicator function is well reconstructed from randomly distributed points ranging $0.5h < \Delta s_l < 1.5h$.

3.1. Effects of h . In this section, we describe the effects of spatial grid size h . Figure 10 shows 4-point delta functions and corresponding indicator functions for different spatial step $h = 1, 0.5$, and 0.25 . We observe that as h is smaller, the delta function becomes sharper and the interface transition layer of the indicator function becomes shorter.

In computational domain $\Omega = (-15, 15) \times (-15, 15)$, we consider uniform immersed boundary points for a circle

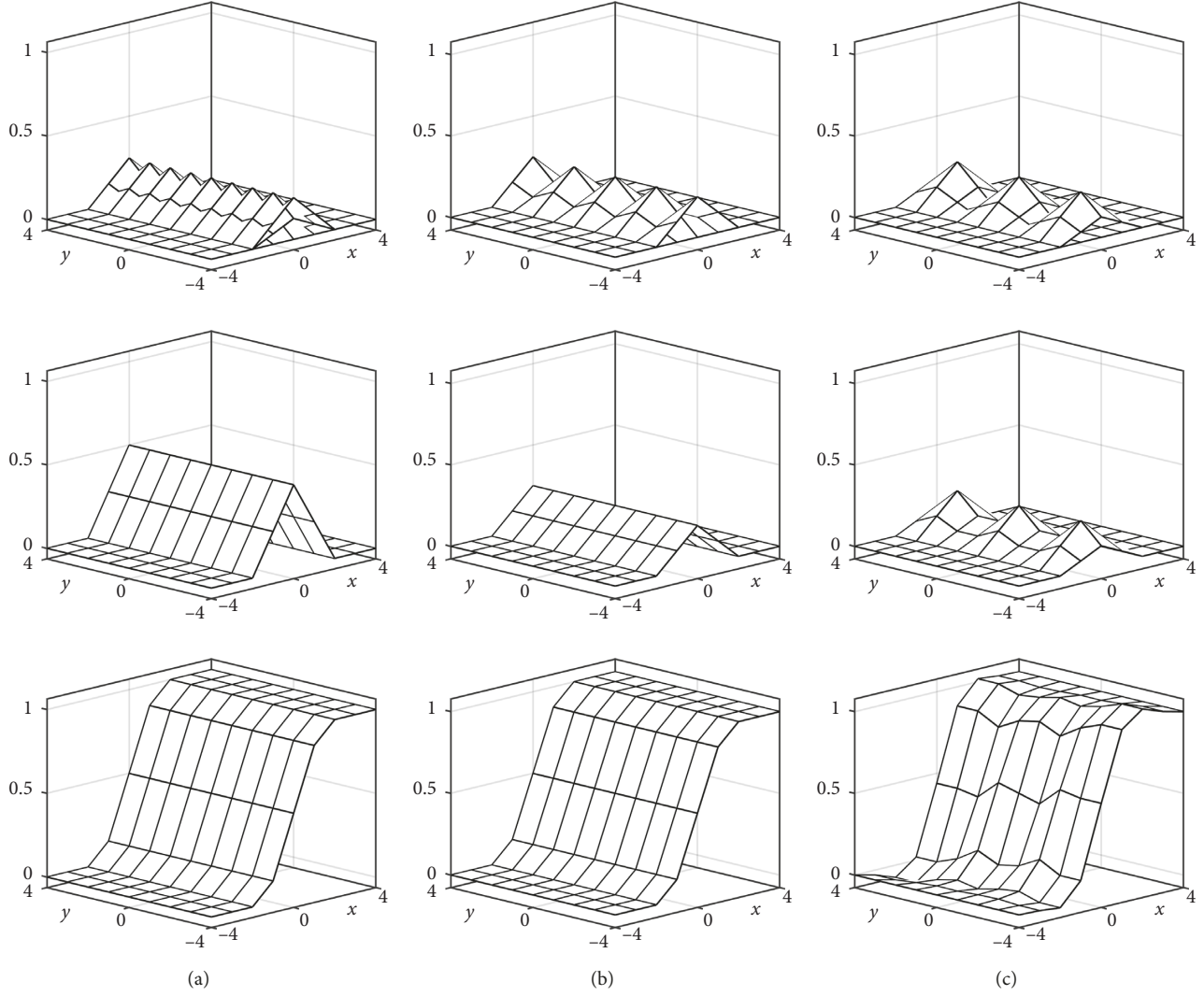


FIGURE 7: From top to bottom row, 2D delta functions $\delta(\mathbf{x} - \mathbf{X}_i) = \delta(x - X_i)\delta(y - Y_i)$ with $X_i = 0$ and $Y_i = \pm\Delta s, \pm 2\Delta s, \dots$, sum of 2D delta functions $\sum_i \delta(\mathbf{x} - \mathbf{X}_i)$, and 2D indicator function $I(\mathbf{x})$: (a) $\Delta s = h$, (b) $\Delta s = 2h$, and (c) $\Delta s = 3h$.

radius of 10 with different $h = 1, 0.5$, and 0.25 as shown in Figure 11(a). In Figure 11(b), we solve the indicator function, accordingly the points in Figure 11(a). It has a more stiff interface as h is smaller. Figure 11(c) shows $\|I^{(k)} - I^{(k-1)}\|_2$ for the Gauss-Seidel iteration with a tolerance $\text{tol} = 1.0e - 6$, where k is the number of iterations and $I^{(0)}$ is a zero vector. We can observe that the number of iterations is getting larger as h approaches zero.

4. Fluid Application

In this section, we give two examples for the applications of indicator function in multiphase flows and fluid-structure interaction (FSI) problem. First, we consider the two-phase flows problem as the dynamics of a droplet suspended in the simple shear flow. The droplet is between two parallel plates as shown in Figure 12. Let $\mathbf{u}(\mathbf{x}, t) = (u(\mathbf{x}, t), v(\mathbf{x}, t))$ be fluid velocity at $\mathbf{x} = (x, y)$ and time t . The Lagrangian variable, denoted as $\mathbf{X}(s, t)$, where s is arc length parameter, expresses the immersed boundary. The governing equations on the domain Ω are as follows:

$$\begin{aligned} \frac{\partial \mathbf{u}(\mathbf{x}, t)}{\partial t} + \mathbf{u}(\mathbf{x}, t) \cdot \nabla \mathbf{u}(\mathbf{x}, t) &= -\nabla p(\mathbf{x}, t) \\ &+ \frac{1}{Re} \Delta \mathbf{u}(\mathbf{x}, t) + \frac{1}{We} \mathbf{f}(\mathbf{x}, t), \end{aligned} \quad (22)$$

$$\nabla \cdot \mathbf{u}(\mathbf{x}, t) = 0,$$

$$\mathbf{f}(\mathbf{x}, t) = \int_{\Gamma} \mathbf{F}(\mathbf{X}(s, t)) \delta^2(\mathbf{x} - \mathbf{X}(s, t)) ds,$$

$$\mathbf{F}(s, t) = \frac{\partial^2 \mathbf{X}(s, t)}{\partial s^2},$$

$$\frac{\partial \mathbf{X}(s, t)}{\partial t} = \mathbf{U}(\mathbf{x}(s, t)),$$

$$\mathbf{U}(\mathbf{X}(s, t)) = \int_{\Omega} \mathbf{u}(\mathbf{x}, t) \delta^2(\mathbf{x} - \mathbf{X}(s, t)) d\mathbf{x}, \quad (23)$$

where Γ is the interface between the two fluids. We define the Reynolds number in equation (22) as $Re = \rho_2 R^2 \dot{\gamma}$,

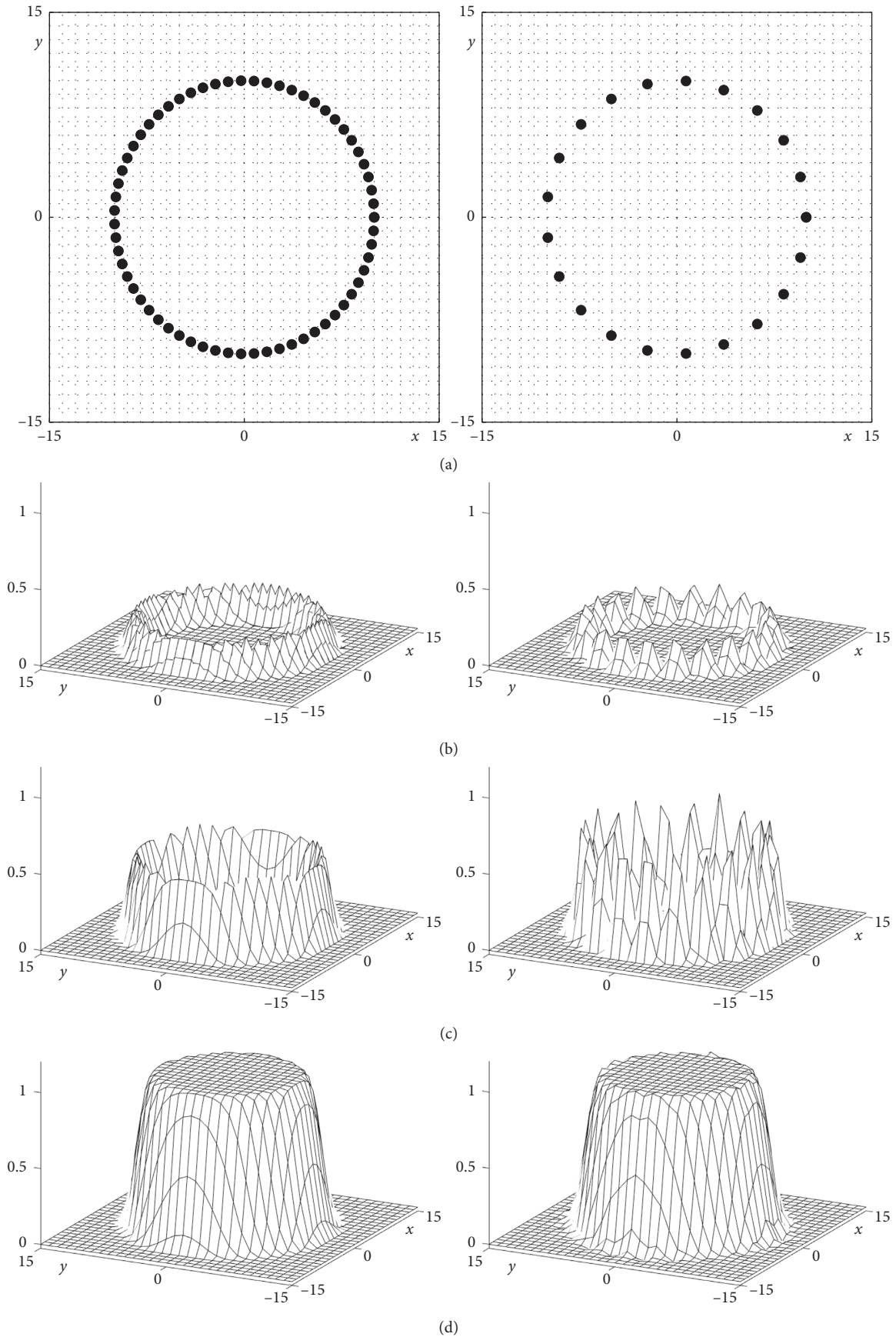


FIGURE 8: (a) Immersed boundary positions with different distance Δs , (b) 2D delta functions of at the boundary positions, (c) sum of 2D delta functions, and (d) 2D indicator function $I(\mathbf{x})$ with different uniform distance Δs .

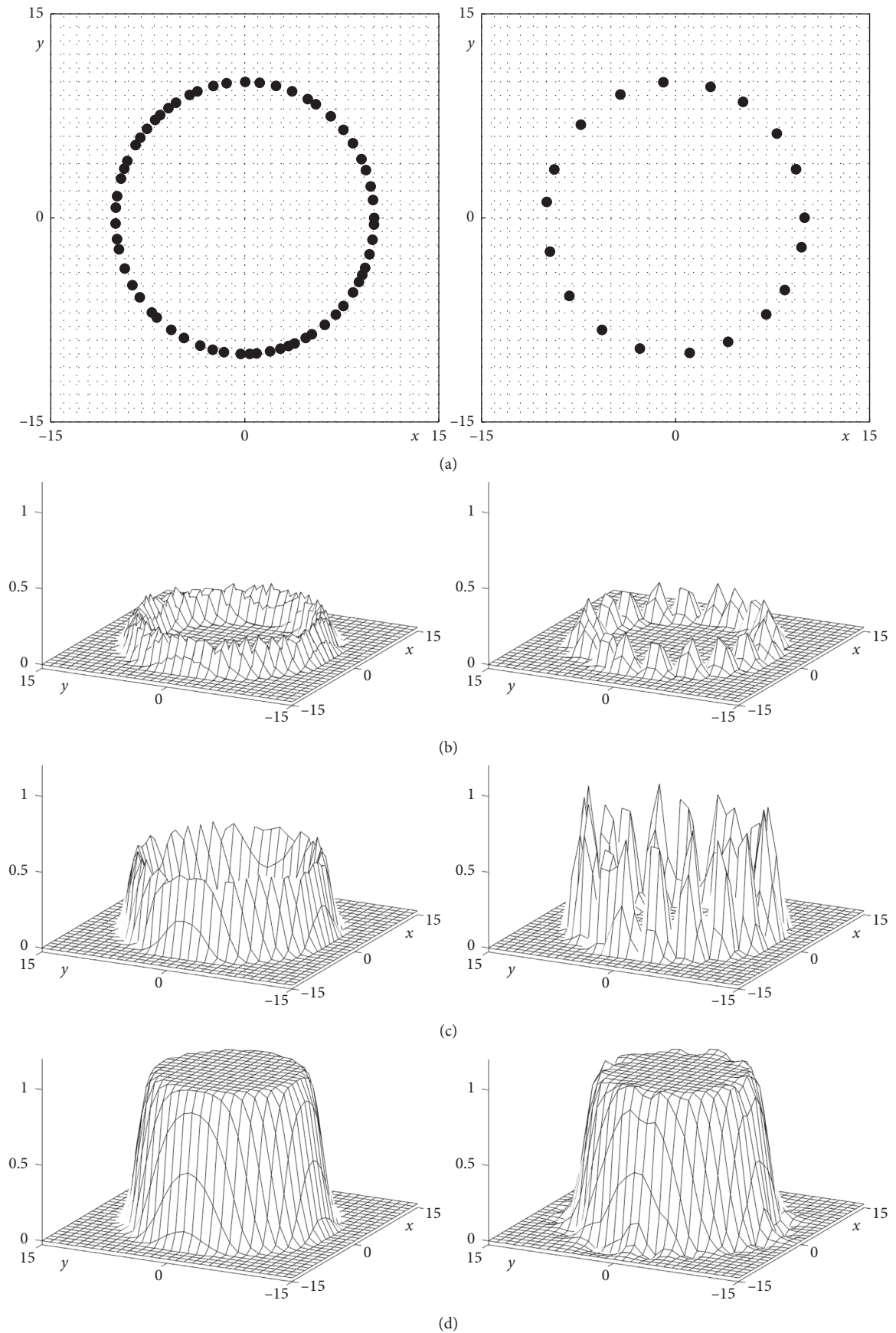


FIGURE 9: (a) Randomly distributed boundary positions, (b) 2D delta functions of boundary positions, (c) sum of 2D delta functions, and (d) 2D indicator function $I(\mathbf{x})$ with different nonuniform distance Δs_j .

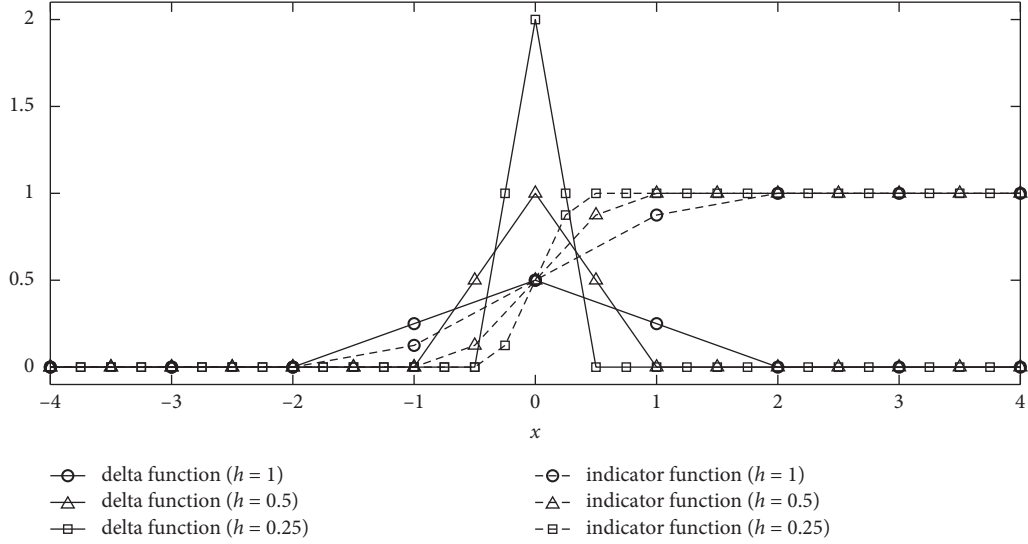


FIGURE 10: Delta and indicator functions with different spatial steps $h = 1, 0.5,$ and 0.25 .

$We = Re \cdot Ca$, and $Ca = \eta R \dot{\gamma} / \sigma$, where ρ is fluid density, η fluid viscosity, R droplet radius, $\dot{\gamma}$ the shear rate, and σ the surface tension coefficient. We define a gradient field,

$$\nabla I(\mathbf{x}, t) = \int_{\Gamma} \mathbf{n}(\mathbf{X}(s, t)) \delta^2(\mathbf{x} - \mathbf{X}(s, t)) ds. \quad (24)$$

To compute the indicator function, the following equation is solved:

$$\Delta I(\mathbf{x}, t) = \nabla \cdot \int_{\Gamma} \mathbf{n}(\mathbf{X}(s, t)) \delta^2(\mathbf{x} - \mathbf{X}(s, t)) ds. \quad (25)$$

Then, the variable density ρ and viscosity μ are defined as follows:

$$\begin{aligned} \rho(I(\mathbf{x}, t)) &= \rho_2 + (\rho_1 - \rho_2)I(\mathbf{x}, t), \\ \mu(I(\mathbf{x}, t)) &= \mu_2 + (\mu_1 - \mu_2)I(\mathbf{x}, t), \end{aligned} \quad (26)$$

where ρ_i and μ_i for $i = 1, 2$ are density and viscosity of fluid i , respectively.

For simplicity, the viscosity and density of the droplet is set equal to that of the matrix phase. Our focus is on the generations of indicator functions from the unit normal of the interface in the drop deformation process. We refer to [37] for the details of numerical algorithms. We consider the simulations of drop deformation on $\Omega = [0, 2] \times [0, 2]$ with a space mesh size 128×128 . A droplet with a radius 0.5 is put into the center of the domain with initially three sets of different Lagrangian points for comparisons. Delta function (5), Reynolds number $Re = 1$, and capillary number $Ca = 0.3$ are used in simulations. We compared three different Δs settings to investigate the effect of Δs on the formation of indicator function at the end time $t = 2.5$. The initial Δs_{ini} values are set to 1.0 h, 5.0 h and 10.0 h with the number of boundary points 201, 38, and 20, separately, see the first column of Figure 13. While the drop deforms, the interface is remeshed by adding and deleting points with the condition $\Delta s_{max} / \Delta s_{min} \leq 2.0$ for different Δs_{ini} leading to the boundary points being more evenly distributed. As the time evolves,

the indicator function could be well resolved for $\Delta s_{ini} = 1.0$ h as shown in the second row of Figure 13. However, increasing Δs will lead the indicator function a slightly serrated border as shown in the second and sixth rows of Figure 13 (case $\Delta s_{ini} = 5.0$ h and 10.0 h), which is unacceptable to separate two immiscible fluids. Moreover, we could see the drop interface shrink in the normal direction quickly by setting the Δs larger while drop deforms in the shear flow, as shown in the odd row of Figure 13. Table 1 lists the area losses as the drop evolves at the time $t = 2.5$. It shows that the larger Δs , the more the drop area loss.

Next, we take the direct-forcing immersed boundary method as an example application in the FSI problem of the indicator function. The nondimensional governing equations are similar to the multiphase flows and read as follows:

$$\frac{\partial \mathbf{u}(\mathbf{x}, t)}{\partial t} + \mathbf{u}(\mathbf{x}, t) \cdot \nabla \mathbf{u}(\mathbf{x}, t) = -\nabla p(\mathbf{x}, t)$$

$$+ \frac{1}{Re} \Delta \mathbf{u}(\mathbf{x}, t) + \mathbf{f}(\mathbf{x}, t),$$

$$\nabla \cdot \mathbf{u}(\mathbf{x}, t) = 0,$$

$$\mathbf{f}(\mathbf{x}, t) = \int_{\Gamma} \mathbf{F}(\mathbf{X}(s)) \delta^2(\mathbf{x} - \mathbf{X}(t)) ds,$$

$$\frac{\partial \mathbf{X}(s)}{\partial t} = \mathbf{U}(\mathbf{X}(s)),$$

$$\mathbf{U}(\mathbf{X}(s)) = \int_{\Omega} \mathbf{u}(\mathbf{x}, t) \delta^2(\mathbf{x} - \mathbf{X}(t)) d\mathbf{x}, \quad (27)$$

where \mathbf{u} is the velocity, p is the pressure, \mathbf{u} is the body force, and Re is the Reynolds number. From equation (27), we can get the following equation:

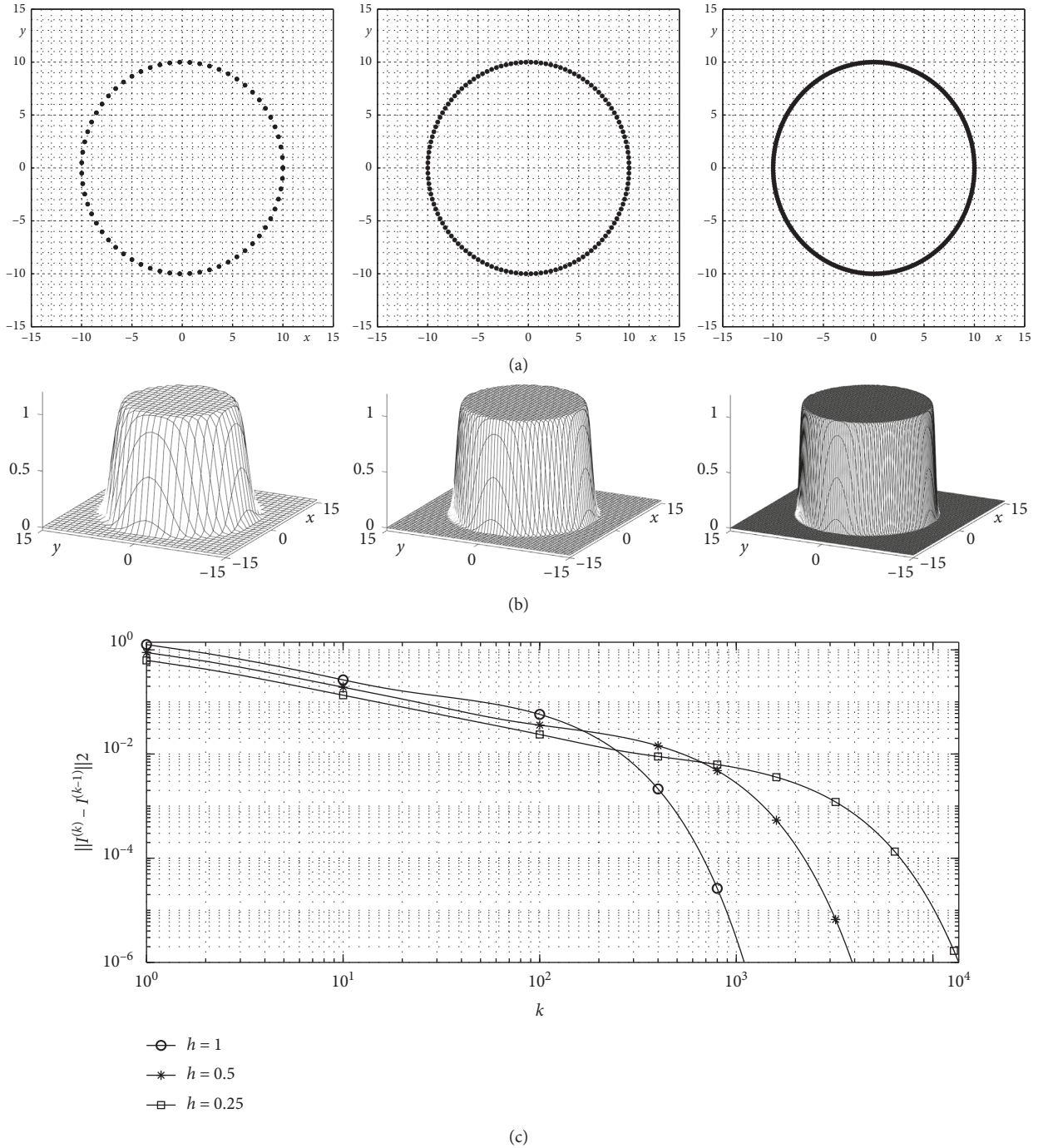


FIGURE 11: (a)-(b) From left to right column, different spatial steps $h = 0.25, 0.5$, and 1 : (a) Lagrangian point X_i and (b) indicator functions. (c) l_2 -error of $I^{(k)}$ and $I^{(k-1)}$ for the number of iterations k using the gauss-seidel method with different spatial steps $h = 1, 0.5$, and 0.25 .

$$\mathbf{f} = \frac{\partial \mathbf{u}}{\partial t} + \mathbf{u} \cdot \nabla \mathbf{u} + \nabla p - \frac{1}{Re} \Delta \mathbf{u} = \frac{\partial \mathbf{u}}{\partial t} - \mathbf{rhs}, \quad (28)$$

$$\frac{\partial \mathbf{u}}{\partial t} - \mathbf{rhs} = \frac{\mathbf{u}^{n+1} - \mathbf{u}^n}{\Delta t} - \mathbf{rhs},$$

where n and $n+1$ are time steps, and $\mathbf{rhs} = -(\mathbf{u} \cdot \nabla \mathbf{u} + \nabla p - 1/Re \Delta \mathbf{u})$. The forcing exerted on the

Lagrangian points at the immersed boundary can be written as follows:

$$\mathbf{F}(\mathbf{X}(s)) = \frac{\mathbf{U}^{n+1}(\mathbf{X}(t)) - \mathbf{U}^*(\mathbf{X}(s))}{\Delta t}, \quad (29)$$

where $\mathbf{U}^{n+1}(\mathbf{X}(s))$ is the desired velocity and $\mathbf{U}^*(\mathbf{X}(s))$ is a temporary velocity of the boundary. The algorithm in detail can be found in [38]. The difference of immersed boundary

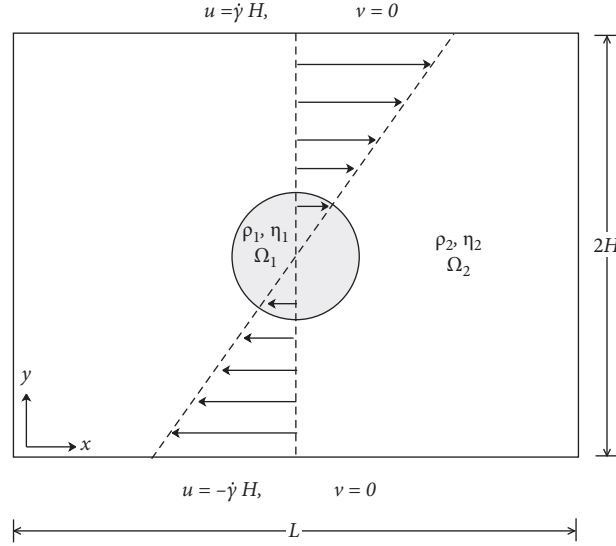


FIGURE 12: Schematic illustration of a liquid droplet.

to handle the multiphase flows and FSI lies on the how to evaluate the boundary force.

For a moving rigid body immersed in the fluid, the imposed force term, the authors in [39] pointed out it

consists of two parts that can be written as the following equations (30) and (31):

$$f_x = \oint_{\partial\Omega} F_x(X(s))ds - \iint_{\Omega} \frac{\partial u}{\partial t} dV \approx \sum_{j=1}^m F_x(X_j)\Delta V_j - \sum_{i=1}^{N_x} \sum_{j=1}^{N_y} \frac{u_{ij}^{n+1} - u_{ij}^n}{\Delta t} I_{ij} \Delta V_{ij}, \quad (30)$$

$$f_y = \oint_{\partial\Omega} F_y(X(s))ds - \iint_{\Omega} \frac{\partial v}{\partial t} dV \approx \sum_{j=1}^m F_y(X_j)\Delta V_j - \sum_{i=1}^{N_x} \sum_{j=1}^{N_y} \frac{v_{ij}^{n+1} - v_{ij}^n}{\Delta t} I_{ij} \Delta V_{ij}, \quad (31)$$

where $\partial\Omega$ is the solid boundary, Ω the solid phase, Δt the time step, I_{ij} the indicator function, u_{ij} , v_{ij} the velocity in Eulerian grid, N_x , N_y the mesh grid numbers, and V_{ij} the mesh volume in ij grid point.

One force in the first terms of right hand sides of equations (30) and (31) is that of a submersed body acting on the external fluid, which can be determined simply by integrating the immersed boundary force densities by equation (29) on the solid boundary that is already evaluated by the direct forcing. Another one that contributes to the unsteady flow inside the solid phase, is the so-called internal or virtual flow force [39] in the second terms of the right hand side of equations (30) and (31). Usually, if the object is fixed in the fluid, we impose the $\mathbf{f} = (f_x, f_y)$ term to satisfy the no-slip boundary condition on the solid surface leading to the second term equals zero. However, when the solid boundary is moving, we should not neglect the effect of the virtual flow, even though its contribution is small [39]. For a complexly enclosed geometry, the indicator function can be used to calculate to its inside virtual flow by letting its value 1, and outside 0 of the moving solid object.

For this moving solid problem in fluid, we consider a 2D NACA0012 airfoil as the representative of a fish body

periodically undulating in the incoming flow. The study of this kind of fish kinematics can be found in [40, 41]. Our focus is on the fish shape expressed by the indicator function. As in the first example of drop deformation in the shear flow, we investigate the effect of Δs on the indicator function. The computational domain is $[0, 4] \times [0, 2]$, with mesh size 256 for y direction. The airfoil is initially represented by 202, 102, and 42 Lagrangian points leading to the point distance Δs is about $0.918h$, $2.117h$, and $6.134h$, where h is the Eulerian grid size. The odd rows of Figure 14 shows the fish undulations with outer normal vectors attached on the boundary points for different Δs settings. Because the boundary deforms not too much, we do not need to remesh it. As shown in Figure 14, by increasing Δs , the indicator functions get zigzag distribution on their boundaries between 0 and 1, which could lead to the calculations of f_x and f_y in equations (30) and (31) a little oscillations. However, the $\Delta s \approx 1.0h$ is good enough to resolve the smooth distribution of indicator function as in the first drop deformation example. It should be noted that the diffused fish interface is not well resolved at the high curvature section of the fishtail for larger Δs as shown in the third case of Figure 14. Letting $\Delta s \approx 1.0h$ resolves it quite well.

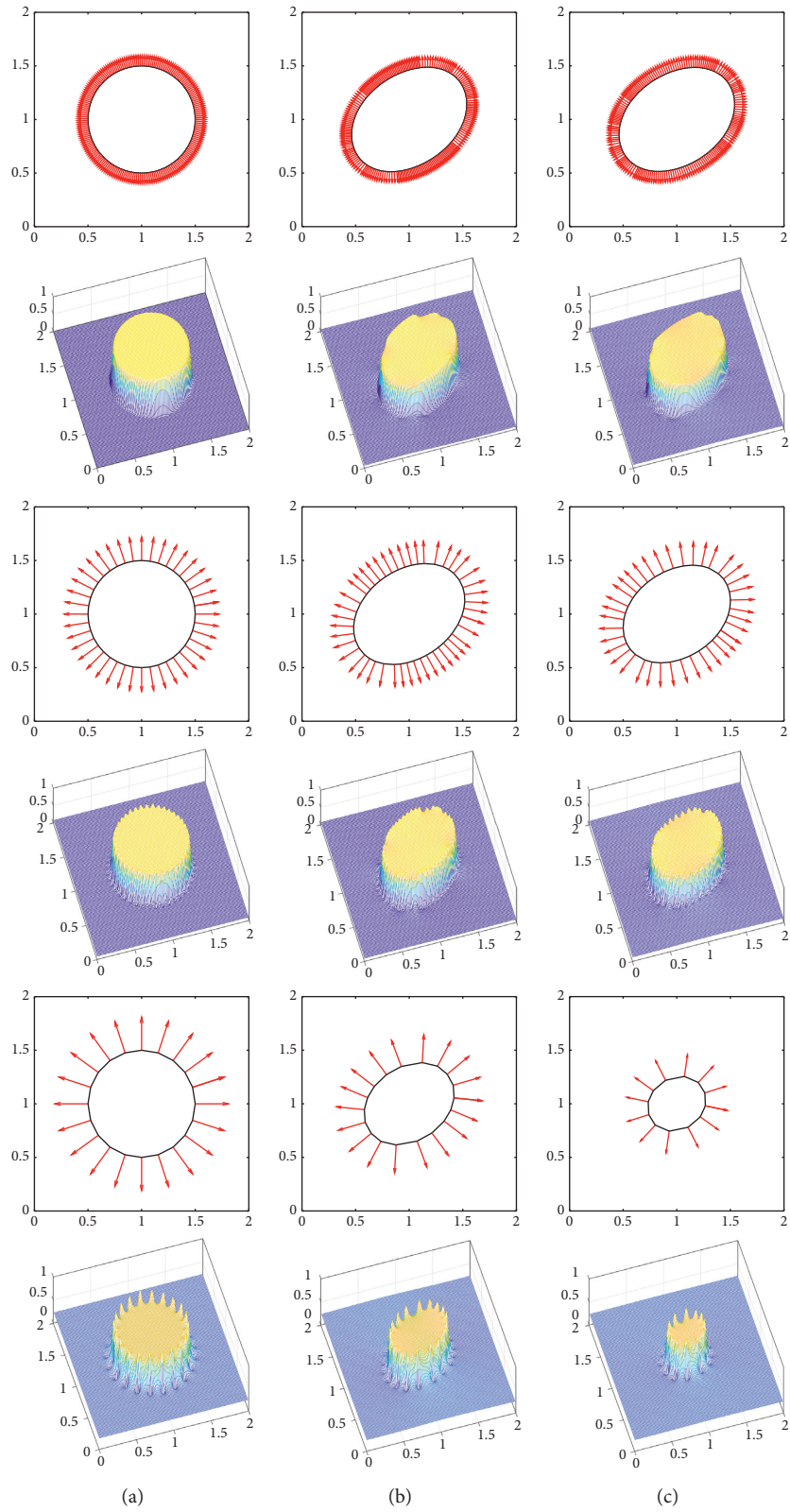


FIGURE 13: From top to bottom, the first, third, and fifth rows are the boundary interfaces with different initial $\Delta s_{ini} = 1.0h, 5.0h$ and $10.0h$ (attached with normal vectors). The even rows are corresponding to theirs' indicator functions. Column (a)–(c), drop evolutions at different times.

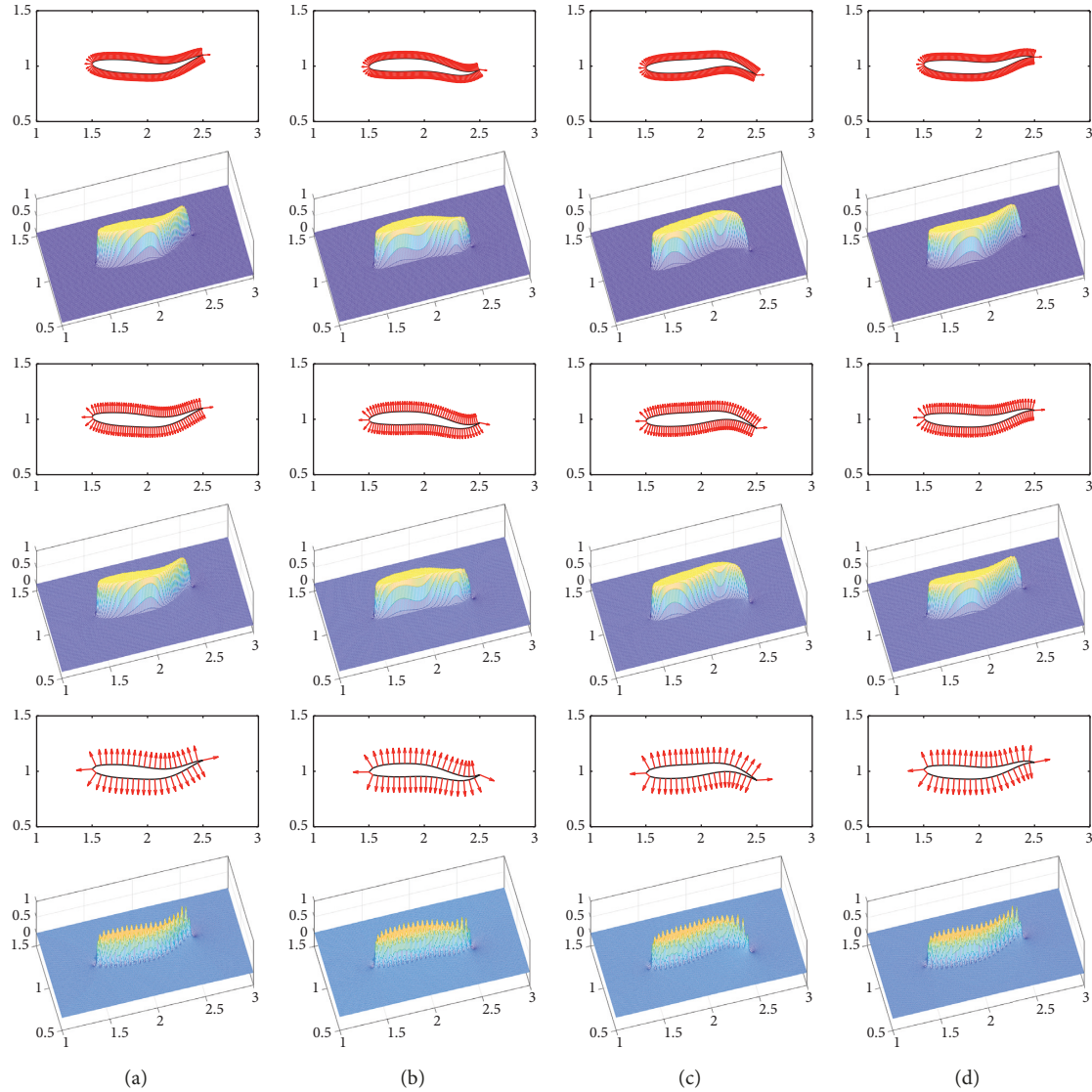


FIGURE 14: From top to bottom, the first, third, and fifth rows are fish boundaries with different initial $\Delta s = 0.918h$, $2.117h$ and $6.134h$ (attached with normal vectors), corresponding to 202, 102, and 42 boundary points. The even rows are corresponding to their indicator functions. Column (a)–(d), fish undulates at different times in a period. (a) $t=0$. (b) $t=0.15$. (c) $t=0.3$. (d) $t=0.45$.

TABLE 1: Drop area loss for the different Δs_{ini} at time $t = 2.5$.

Δs_{ini}	1.0 h	5.0 h	10.0 h
Initial area	0.7852	0.7822	0.7725
Final area	0.7852	0.6856	0.2070
Area loss (%)	0.0	12.35	73.20

5. Conclusion

In this article, we presented a detailed derivation and numerical investigation of an indicator function together with its fluid applications in the immersed boundary method. We used the discrete Dirac delta function to construct an indicator function from a set of Lagrangian points. We solved the resulting discrete Poisson equation with the zero Dirichlet boundary condition using an iterative method. We

presented several computational tests to study the effect of parameters such as distance between points, uniformity of the distance, and types of the Dirac delta functions on the indicator function. Two applications indicate that the construction of the indicator function are effective, multi-purpose, and easy-to-use in separating the changing phases. We note that the indicator function can be extended directly and readily to the three-dimensional space. Based on the above-given numerical investigations, as future works, we

believe that investigation of the 3D indicator function has more practical values.

Data Availability

No data were used to support this study.

Conflicts of Interest

The authors declare that there are no conflicts of interest.

Acknowledgments

The study was supported by Brain Korea 21 FOUR from the Ministry of Education of the Republic of Korea.

References

- [1] R. Abadi, A. Fakhari, and M. H. Rahimian, "Phase-change modeling based on a novel conservative phase-field method," *Journal of Computational Physics*, vol. 432, Article ID 110111, 2021.
- [2] Y. Vasilopoulos, "An alternative phase-field interfacial tension force representation for binary fluid systems," *Physics of Fluids*, vol. 32, no. 10, Article ID 102101, 2020.
- [3] J. Yang and J. Kim, "A phase-field method for two-phase fluid flow in arbitrary domains," *Computers & Mathematics with Applications*, vol. 79, no. 6, pp. 1857–1874, 2020.
- [4] Z. Yang, C. Zhong, and C. Zhuo, "Phase-field method based on discrete unified gas-kinetic scheme for large-density-ratio two-phase flows," *Physical Review*, vol. 99, no. 4, Article ID 043302, 2019.
- [5] L. Cappanera, J. L. Guermont, W. Herreman, and C. Nore, "Momentum-based approximation of incompressible multiphase fluid flows," *International Journal for Numerical Methods in Fluids*, vol. 86, no. 8, pp. 541–563, 2018.
- [6] T. J. Moroney, D. R. Lusmore, S. W. McCue, and D. S. McElwain, "Extending fields in a level set method by solving a biharmonic equation," *Journal of Computational Physics*, vol. 343, pp. 170–185, 2017.
- [7] S. Osher and R. P. Fedkiw, "Level set methods: an overview and some recent results," *Journal of Computational Physics*, vol. 169, no. 2, pp. 463–502, 2001.
- [8] M. Kanchan and R. Maniyeri, "Numerical simulation of buckling and asymmetric behavior of flexible filament using temporal second-order immersed boundary method," *International Journal of Numerical Methods for Heat and Fluid Flow*, vol. 30, no. 3, pp. 1047–1095, 2019.
- [9] U. Dutta, S. Sarkar, A. Baruah, and N. Mandal, "Ascent modes of jets and plumes in a stationary fluid of contrasting viscosity," *International Journal of Multiphase Flow*, vol. 63, pp. 1–10, 2014.
- [10] G. D. Weymouth and D. P. Yue, "Conservative volume-of-fluid method for free-surface simulations on cartesian-grids," *Journal of Computational Physics*, vol. 229, no. 8, pp. 2853–2865, 2010.
- [11] M. Berardi, F. Difonzo, and L. Lopez, "A mixed MoL-TMoL for the numerical solution of the 2D Richards' equation in layered soils," *Computers & Mathematics with Applications*, vol. 79, no. 7, pp. 1990–2001, 2020.
- [12] L. Furnari, A. Senatore, A. De Rango, M. De Biase, S. Straface, and G. Mendicino, "Asynchronous cellular automata sub-surface flow simulations in two- and three-dimensional heterogeneous soils," *Advances in Water Resources*, vol. 153, Article ID 103952, 2021.
- [13] Z. Li, L. Wang, E. Aspinwall et al., "Some new analysis results for a class of interface problems," *Mathematical Methods in the Applied Sciences*, vol. 38, no. 18, pp. 4530–4539, 2015.
- [14] A. Agarwal, G. Singh, and A. Prakash, "Numerical investigation of flow behavior in double-rushton turbine stirred tank bioreactor," *Materials Today Proceedings*, vol. 43, pp. 51–57, 2021.
- [15] Y. Inoue, K. Ishida, N. Takada, and M. Hojo, "Reductions in anisotropic errors from implementation of phase-field wetting boundary condition for off-grid objects," *International Journal of Computational Methods*, vol. 12, no. 06, Article ID 1550042, 2015.
- [16] C. S. Peskin, "Numerical analysis of blood flow in the heart," *Journal of Computational Physics*, vol. 25, no. 3, pp. 220–252, 1977.
- [17] R. Abadi, M. H. Rahimian, and A. Fakhari, "Conservative phase-field lattice-Boltzmann model for ternary fluids," *Journal of Computational Physics*, vol. 374, pp. 668–691, 2018.
- [18] A. De Rosis and E. Enan, "A three-dimensional phase-field lattice Boltzmann method for incompressible two-components flows," *Physics of Fluids*, vol. 33, no. 4, Article ID 043315, 2021.
- [19] H. Yazdi, M. H. Rahimiani, and H. Safari, "Numerical simulation of pressure-driven phase-change in two-phase fluid flows using the Lattice Boltzmann Method," *Computers & Fluids*, vol. 172, pp. 8–18, 2018.
- [20] D. B. Zhakebayev, B. A. Satenova, and D. S. Agadayeva, "Lattice-Boltzmann Method for Simulating Two-component Fluid Flows," *International Journal of Mathematics and Physics*, vol. 11, no. 2, pp. 32–40, 2020.
- [21] G. Tryggvason, B. Bunner, A. Esmaeeli et al., "A front-tracking method for the computations of multiphase flow," *Journal of Computational Physics*, vol. 169, no. 2, pp. 708–759, 2001.
- [22] X. Shang, Z. Luo, E. Y. Gatapova, O. A. Kabov, and B. Bai, "GNBC-based front-tracking method for the three-dimensional simulation of droplet motion on a solid surface," *Computers & Fluids*, vol. 172, pp. 181–195, 2018.
- [23] G. Tryggvason, B. Bunner, O. Ebrat, and W. Tauber, *Computations of Multiphase Flows by a Finite Difference/front Tracking Method, I. Multi-Fluid Flows*, p. 7, Lecture Series-von Karman Institute For Fluid Dynamics, Sint-Genesius-Rode, Belgium, 1998.
- [24] K. Y. Chen, K. A. Feng, Y. Kim, and M. C. Lai, "A note on pressure accuracy in immersed boundary method for Stokes flow," *Journal of Computational Physics*, vol. 230, no. 12, pp. 4377–4383, 2011.
- [25] C. R. Ong and H. Miura, "Immersed boundary method with irrotational discrete delta vector for droplet simulations of large density ratio," *Journal of Computational Physics*, vol. 391, pp. 280–302, 2019.
- [26] Y. Seol, Y. H. Tseng, Y. Kim, and M. C. Lai, "An immersed boundary method for simulating Newtonian vesicles in viscoelastic fluid," *Journal of Computational Physics*, vol. 376, pp. 1009–1027, 2019.
- [27] M. Kumar and G. Natarajan, "Diffuse-interface immersed-boundary framework for conjugate-heat-transfer problems," *Physical Review*, vol. 99, no. 5, Article ID 053304, 2019.
- [28] A. Spizzichino, S. Goldring, and Y. Feldman, "Prediction of the structure and refractive index profile of fused fiber-optic components: A numerical and experimental study," *Physical Review*, vol. 103, no. 1, Article ID 013315, 2021.

- [29] B. E. Griffith and C. S. Peskin, "On the order of accuracy of the immersed boundary method: higher order convergence rates for sufficiently smooth problems," *Journal of Computational Physics*, vol. 208, no. 1, pp. 75–105, 2005.
- [30] C. S. Peskin, "The immersed boundary method," *Acta Numerica*, vol. 11, pp. 479–517, 2002.
- [31] S. J. Shin, W. X. Huang, and H. J. Sung, "Assessment of regularized delta functions and feedback forcing schemes for an immersed boundary method," *International Journal for Numerical Methods in Fluids*, vol. 58, no. 3, pp. 263–286, 2008.
- [32] X. Yang, X. Zhang, Z. Li, and G. W. He, "A smoothing technique for discrete delta functions with application to immersed boundary method in moving boundary simulations," *Journal of Computational Physics*, vol. 228, no. 20, pp. 7821–7836, 2009.
- [33] R. J. LeVeque and Z. Li, "The immersed interface method for elliptic equations with discontinuous coefficients and singular sources," *SIAM Journal on Numerical Analysis*, vol. 31, no. 4, pp. 1019–1044, 1994.
- [34] A. M. Roma, C. S. Peskin, and M. J. Berger, "An adaptive version of the immersed boundary method," *Journal of Computational Physics*, vol. 153, no. 2, pp. 509–534, 1999.
- [35] B. E. Griffith, R. D. Hornung, D. M. McQueen, and C. S. Peskin, "An adaptive, formally second order accurate version of the immersed boundary method," *Journal of Computational Physics*, vol. 223, no. 1, pp. 10–49, 2007.
- [36] J. M. Stockie, "Analysis and Computation of Immersed Boundaries, with Application to Pulp Fibres," Doctoral dissertation, University of British Columbia, Vancouver, BC, Canada, 1997.
- [37] Y. Li, E. Jung, W. Lee, H. G. Lee, and J. Kim, "Volume preserving immersed boundary methods for two-phase fluid flows," *International Journal for Numerical Methods in Fluids*, vol. 69, no. 4, pp. 842–858, 2012.
- [38] Z. Wang, J. Fan, and K. Luo, "Combined multi-direct forcing and immersed boundary method for simulating flows with moving particles," *International Journal of Multiphase Flow*, vol. 34, no. 3, pp. 283–302, 2008.
- [39] L. Shen, E. S. Chan, and P. Lin, "Calculation of hydrodynamic forces acting on a submerged moving object using immersed boundary method," *Computers & Fluids*, vol. 38, no. 3, pp. 691–702, 2009.
- [40] G. J. Dong and X. Y. Lu, "Characteristics of flow over traveling wavy foils in a side-by-side arrangement," *Physics of Fluids*, vol. 19, no. 5, Article ID 057107, 2007.
- [41] M. S. Khalid, I. Akhtar, and H. Dong, "Hydrodynamics of a tandem fish school with asynchronous undulation of individuals," *Journal of Fluids and Structures*, vol. 66, pp. 19–35, 2016.